

Generation of angular-momentum-dominated electron beams from a photoinjector

Y.-E. Sun,^{1,*} P. Piot,^{2,†}

K.-J. Kim,^{3,‡} N. Barov,^{4,§} S. Lidia,⁵ J. Santucci,² R. Tikhoplav,⁶ and J. Wennerberg^{2,¶}

¹*University of Chicago, Chicago, IL 60637, USA*

²*Fermi National Accelerator Laboratory, Batavia, IL 60510, USA*

³*Argonne National Laboratory, Argonne, IL 60439, USA*

⁴*Northern Illinois University, DeKalb, IL 60115, USA*

⁵*Lawrence Berkeley National Laboratory, Berkeley, CA 94720, USA*

⁶*University of Rochester, Rochester, NY 14627, USA*

(Dated: March 31, 2022)

Abstract

Various projects under study require an angular-momentum-dominated electron beam generated by a photoinjector. Some of the proposals directly use the angular-momentum-dominated beams (e.g. electron cooling of heavy ions), while others require the beam to be transformed into a flat beam (e.g. possible electron injectors for light sources and linear colliders). In this paper, we report our experimental study of an angular-momentum-dominated beam produced in a photoinjector, addressing the dependencies of angular momentum on initial conditions. We also briefly discuss the removal of angular momentum. The results of the experiment, carried out at the Fermilab/NICADD Photoinjector Laboratory, are found to be in good agreement with theoretical and numerical models.

PACS numbers: 29.27.-a, 41.85.-p, 41.75.Fr

*Corresponding author. Electronic address: yinesun@uchicago.edu

†Corresponding author. Electronic address: piot@fnal.gov

‡Also at University of Chicago, Chicago, IL 60637, USA

§Now at Far-tech Inc, San Diego, CA 92121, USA

¶Now at Purdue University, West Lafayette, IN 47907, USA

I. INTRODUCTION

Angular-momentum-dominated electron beams generated by photoinjectors have direct applications in several accelerator proposals presently under consideration, either in the field of high-energy colliders or accelerator-based light sources. In Reference [1], an angular-momentum-dominated, or “magnetized”, beam is proposed to be accelerated to ~ 50 MeV and used for electron beam cooling [2, 3] of ion beams in the relativistic heavy ion collider (RHIC). In such a scheme, the electron beam propagates together with the ion beam at the same velocity. Collisions of ions with electrons lead to a transfer of thermal motion from the ion to the electron beam. As the two beams co-propagate, the electron-ion effective interaction length is increased due to the helical trajectory of the electron in the magnetic field, thereby improving the cooling efficiency. The cooling rate is then mainly determined by the longitudinal momentum spread of the electron beam, which can be made much smaller than the transverse one. Reference [4] concerns the photoinjector production of flat beams, i.e. a beam with high transverse emittance ratio. The technique consists of manipulating an angular-momentum-dominated beam produced by a photoinjector using the linear transformation described in Reference [5]. The latter linear transformation removes the angular momentum and results in a flat beam. In the context of linear collider proposals, where a flat beam at the interaction point is needed to reduce beamstrahlung [6], the development of a flat-beam electron source is an attractive idea since it could simplify or eliminate the need for an electron damping ring. The flat beam technique is also proposed for generation of ultrashort X-ray pulses by making use of the smaller dimension of the flat beam [7], and also in enhancing beam-surface interaction in a Smith-Purcell radiator [8] or in an image charge undulator [9]. A proof-of-principle experiment conducted at the Fermilab/NICADD Photoinjector Laboratory (FNPL)[29] has demonstrated the flat beam production [10, 11], where an emittance ratio of 50 was reported.

In this paper we report on recent results pertaining to the experimental investigation of some properties of an angular-momentum-dominated beam. We also briefly address the removal of angular momentum and the subsequent generation of a flat beam. Producing flat beams is our primary motivation for the present studies.

In Section II we briefly summarize theoretical aspects of the photoinjector production of angular-momentum-dominated beams. In Section III we describe the experimental set-up

of FNPL. Sections IV and V are dedicated to experimental results and their comparisons to theory and numerical simulations. Our conclusions appear in Section VI.

II. THEORETICAL BACKGROUND

In this section we assume the beam and external focusing forces to be cylindrically symmetric. The cylindrical symmetry implies the conservation of the canonical angular momentum of each electron. In an axial magneto static field $B_z(z)$, the canonical angular momentum of an electron, L , in circular cylindrical coordinates (r, ϕ, z) is [12]

$$L = \gamma m r^2 \dot{\phi} + \frac{1}{2} e B_z(z) r^2, \quad (1)$$

where γ is the Lorentz factor, $\dot{\phi}$ the time derivative of ϕ , m and e are respectively the electron rest mass and charge.

The average canonical angular momentum of the electrons, $\langle L \rangle$, is obtained by averaging Eq. (1) over the beam distribution. At the photocathode location, we have $\langle \dot{\phi} \rangle = 0$ and

$$\langle L \rangle = \frac{1}{2} e B_0 \langle r^2 \rangle = e B_0 \sigma_c^2, \quad (2)$$

where $\sigma_c = \sqrt{\langle r^2 \rangle / 2}$ is the transverse root-mean-square (rms) beam size on the photocathode, $B_0 = B_z(z = 0)$ is the axial magnetic field on the photocathode.

Outside the solenoidal field region, where B_z vanishes, an electron acquires mechanical angular momentum due to the torque exerted on it in the transition region. Since $B_z(z) = 0$, the second term of Eq. (1) vanishes and the canonical angular momentum is given by the first term of Eq. (1), which is the mechanical angular momentum. It is convenient to normalize $\langle L \rangle$ with the axial momentum p_z , and introduce the quantity \mathcal{L} given by

$$\mathcal{L} = \frac{\langle L \rangle}{2 p_z} = \kappa \sigma_c^2, \quad (3)$$

where $\kappa = e B_0 / (2 p_z)$.

The beam angular momentum can be removed by means of a properly designed skew quadrupole section [13, 14, 15] and the beam is transformed into a flat beam (see section V). The flat beam transverse emittances after the skew quadrupole section, ϵ_{\pm} , are given by [15, 16]:

$$\epsilon_{\pm} = \sqrt{\epsilon_u^2 + \mathcal{L}^2} \pm \mathcal{L}. \quad (4)$$

Here ϵ_u is the uncorrelated transverse emittance prior to the skew quadrupole section. Note that the four dimensional emittance is conserved since $\epsilon_u^2 = \epsilon_+ \epsilon_-$.

The evolution of the transverse rms beam size of a relativistic electron bunch in a drift is given by the envelope equation [17]

$$\sigma'' - \frac{K}{4\sigma} - \frac{\epsilon_u^2}{\sigma^3} - \frac{\mathcal{L}^2}{\sigma^3} = 0, \quad (5)$$

where σ is the transverse rms size, $K = \frac{2I}{I_0\gamma^3}$ is the generalized perveance, I is the absolute value of the instantaneous beam current and I_0 is the Alfvén current for electrons (~ 17 kA). The second, third and fourth terms respectively represent the effects due to space charge, emittance and the angular momentum. For low energy beam, the space charge term is important. However, for the typical operating conditions considered in this paper, e.g., $\gamma \approx 30$, bunch charge ≈ 0.5 nC, rms beam duration $\sigma_t \approx 4$ ps, $\sigma \approx 1.25$ mm [18], $\gamma\epsilon_u \approx 4$ mm mrad [19], $\gamma\mathcal{L} \approx 20$ mm mrad, the fourth term Eq. 5 is much greater than the second and the third term. Such a beam is said to be angular momentum dominated.

III. EXPERIMENTAL SETUP

The experimental production and characterization of angular-momentum-dominated

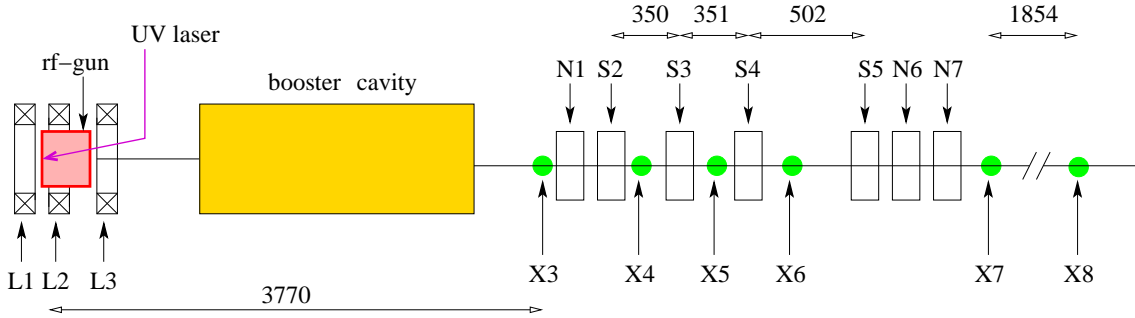


FIG. 1: Overview of the FNPL beamline. Here only the elements pertaining to the flat-beam experiment are shown. The letters represents solenoidal magnetic lenses (L), normal (N) and skew (S) quadrupoles, and diagnostic stations (X). Dimensions are in mm.

electron beams were carried out at FNPL.

The photoinjector incorporates a photoemission source consisting of a $1 + \frac{1}{2}$ cell cavity operating at 1.3 GHz, the so-called radio frequency (rf) gun. An ultraviolet (UV) laser impinges a cesium telluride photocathode located on the back plate of the rf gun half cell.

The thereby photoemitted electron bunch exits from the rf-gun at 4 MeV/c and is immediately injected into a TESLA-type superconducting cavity [20] (henceforth referred to as the booster cavity). The bunch momentum downstream of the booster cavity is approximately 16 MeV/c when the cavity is operated to yield the maximum energy gain. The typical operating conditions of the main subsystems of the photoinjector are gathered in Table I, and a block diagram of the facility is depicted in Fig. 1.

The transverse size of the UV drive-laser at the photocathode is set by a remotely controllable iris. The laser temporal profile is a Gaussian distribution with rms duration of ~ 3.5 ps.

The rf gun is surrounded by three solenoidal magnetic lenses independently powered. This allows proper focusing of the electron bunch while maintaining the desired magnetic field on the photocathode.

Downstream of the booster cavity, the beamline includes a round-to-flat-beam (RTFB) transformer, consisting of four skew quadrupoles, that can be used to remove the mechanical angular momentum.

Several optical transition radiation (OTR) or fluorescent (YAG-based) screens serve as diagnostics to measure the beam's transverse density at various locations in the beamline. Transverse emittances can also be measured based on the multislit [21, 22], or quadrupole scan techniques [23]. The multislit mask used for emittance measurements consists of a 6-mm-thick tungsten mask with 48 μm -wide slits spaced 1 mm apart.

parameter	value	units
laser injection phase	25 ± 5	rf-deg
laser radius on cathode	$[0.6, 1.6] \pm 0.05$	mm
laser pulse duration	3.5 ± 0.5	ps
bunch charge	$[0.2, 1.6]$	nC
E_z on cathode	35 ± 0.2	MV/m
B_0 on cathode	$[200, 1000]$	Gauss
booster cavity acc. gradient	~ 12	MV/m

TABLE I: Typical settings for the photocathode drive laser, rf gun, and accelerating section. Values in square brackets correspond to the range used in the measurements.

IV. MEASUREMENTS OF CANONICAL ANGULAR MOMENTUM

We now turn to the basic properties of the canonical angular momentum. We especially investigate the conversion of the canonical angular momentum of the photo-emitted electron bunch into mechanical angular momentum downstream of the booster cavity.

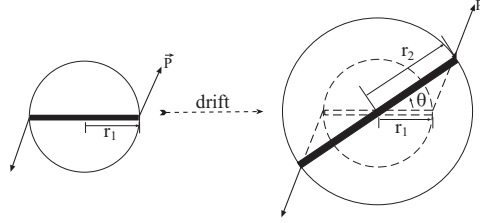


FIG. 2: Beam with angular-momentum-induced shearing while drifting. The dark narrow rectangle represents a slit inserted into the beamline to measure the shearing angle (see text for more details).

The canonical angular momentum at the photocathode surface is obtained from Eq. (2). Given the experimental settings of the solenoidal lens currents, the magnetic field, B_0 , is inferred via simulations using the POISSON [24] program, which is bench-marked against calibration of the solenoidal lenses [25]. The value of σ_c used in Eq. (2) is directly measured from an image of the UV laser on a “virtual photocathode”. The virtual photocathode is a calibrated UV-sensitive screen, located outside of the vacuum chamber, being a one-to-one optical image of the photocathode.

To elaborate the method used to measure the mechanical angular momentum downstream of the booster cavity, we consider an electron in a magnetic-field-free region at longitudinal location z_1 with transverse radial vector $\mathbf{r}_1 = r_1 \hat{\mathbf{e}}_x$ ($\hat{\mathbf{e}}_x$ stands for the x -axis unit vector). After propagating through a drift space, the electron reaches \mathbf{r}_2 at location z_2 . Let $\theta = \angle(\mathbf{r}_1, \mathbf{r}_2)$ be the angle between the two aforementioned radial vectors (θ is henceforth referred to as “shearing angle”; see Fig. 2). The mechanical angular momentum of the electron, \mathbf{L} , is given by:

$$\mathbf{L} = r_1 \hat{\mathbf{e}}_x \times \mathbf{P} = r_1 p_y \hat{\mathbf{e}}_x \times \hat{\mathbf{e}}_y. \quad (6)$$

By introducing $y' = \frac{dy}{dz} = \frac{p_y}{p_z}$, where p_y is the vertical component of the momentum, and noting that y' is a constant in a drift space for an angular-momentum-dominated beam, we

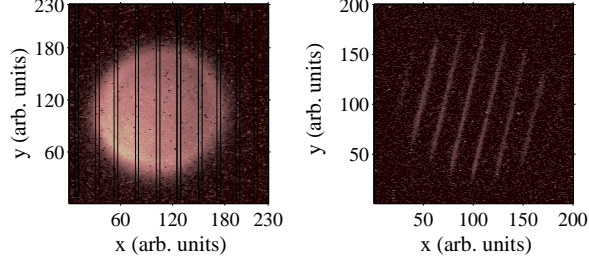


FIG. 3: Example of data set used for mechanical angular momentum measurement. Beam transverse density on X3 (left) and observed beamlets on X6 when the vertical multislit mask is inserted at X3 (right). The vertical lines superimposed on the X3 image is an illustration of vertical slits when the multislit mask is inserted.

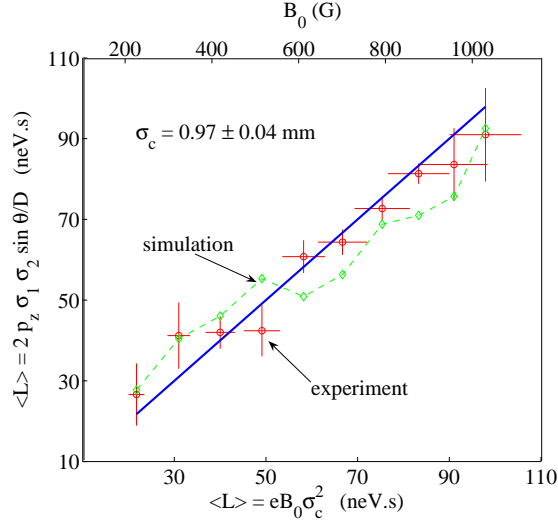


FIG. 4: Mechanical angular momentum from Eq. (8) versus the canonical angular momentum calculated from Eq. (2). The labels “experiment” and “simulation” correspond respectively to experimentally measured data points and simulated values found by modeling of the measurement technique. The solid diagonal line is drawn simply to aid the eye.

see that the change in vertical coordinate is $\Delta y = y' D = r_2 \sin \theta$ (see Fig. 2). Hence Eq. (6) can be rewritten in the convenient form

$$\mathbf{L} = r_1 p_z y' \hat{\mathbf{e}}_z = p_z \frac{r_1 r_2 \sin \theta}{D} \hat{\mathbf{e}}_z. \quad (7)$$

For a cylindrically symmetric laminar beam with rms transverse beam sizes σ_1 and σ_2 at respective locations z_1 and z_2 along the beamline, the averaged mechanical angular momentum

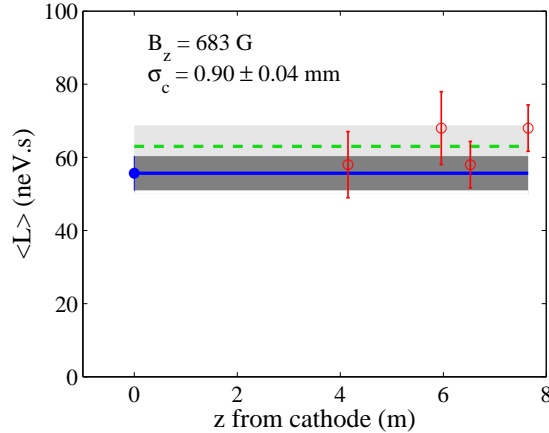


FIG. 5: Evolution of canonical angular momentum along the beamline. At photocathode location (dot), canonical angular momentum is calculated from Eq. (2) and solid line is this value extended along z . At other locations (circles), mechanical angular momentum is obtained from Eq. (8) and the dashed line is the average. The shaded area covers the uncertainties in the measurements either from Eq. (2) (darker strip) or from Eq. (8) (lighter strip).

can then be calculated via

$$\langle L \rangle = 2p_z \frac{\sigma_1 \sigma_2 \sin \theta}{D}. \quad (8)$$

Thus the measurements of rms beam sizes at locations z_1 and z_2 along with the corresponding shearing angle provide all the necessary information for calculating the mechanical angular momentum. Experimentally, the shearing angle is obtained by inserting at location z_1 a multislit mask and measuring the corresponding shearing angle of the beamlets at the location z_2 ; see Fig. 3. For the mechanical angular momentum measurement reported here we use the diagnostic stations X3 and X6 (see Fig. 1). The X3 diagnostic station includes an OTR screen and two insertable multislit masks (with vertical and horizontal slits). The station X6 is only equipped with an OTR screen.

A set of measurements of mechanical angular momentum versus B_0 was reported in Ref. [26]. In the present Paper, such measurements are performed by varying B_0 over a wider range ($B_0 \in [200, 1000]$ Gauss for a bunch charge of $0.41 \pm 0.05 \text{ nC}$; see details in Ref. [18]). The measurement technique discussed in the previous paragraph was also numerically tested for each experimental data point. In Fig. 4 we compare the measured mechanical angular momentum from Eq. (8) with the canonical angular momentum calculated from Eq. (2), given the B_0 . The measured values include both experimental data and simulated values,

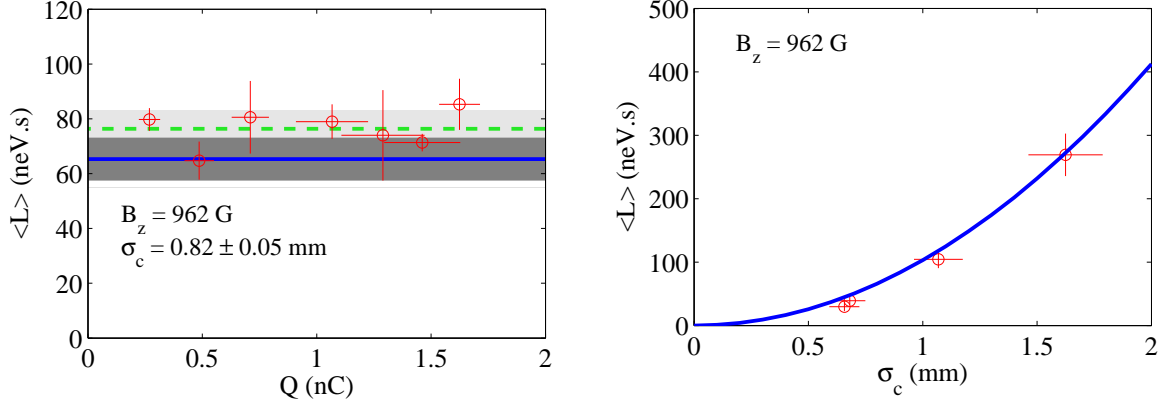


FIG. 6: Canonical angular momentum versus charge (top) and photocathode drive-laser spot size (bottom). The measured mechanical angular momenta (circles) are compared with the theoretical value of the canonical angular momentum calculated from the axial magnetic field (solid line). In the top figure, the dashed line represents the average value of all the data points, and the shaded area has the same meaning as in Fig. 5.

i.e., values that have been retrieved after simulating the measurement technique numerically with the particle tracking program ASTRA [27]. The uncertainties in the measurement of angular momentum are obtained via error propagation from the direct measurements of rms beam sizes and the “shearing angle”.

Conservation of canonical angular momentum is demonstrated in Fig. 5, where the angular momentum was measured at different locations along the beamline. In these measurements all quadrupoles are turned off so that the beam propagated in a drift space.

The dependence of mechanical angular momentum on the charge was also explored. In this experiment, the laser spot size was set to $\sigma_c = 0.82$ mm, and the laser intensity was varied via a wave-plate attenuator located in the UV laser path. The results, shown in Fig. 6(a), indicate the mechanical angular momentum, for our set of operating parameters, is charge-independent, confirming our assumption that the beam dynamics is angular-momentum-dominated in the range explored here.

Finally the dependence of canonical angular momentum versus σ_c was investigated. The laser intensity was held constant and B_0 was identical to the previous experiment ($B_0 = 962$ G). The charge density in the bunch is therefore kept constant. The measurements [see Fig. 6(b)] support the expected quadratic dependence of the angular momentum on σ_c

indicated in Eq. (2).

The measured dependencies of canonical angular momentum on the different parameters are all in good agreement with theoretical expectations. Such an agreement gives us some confidence on our ability to control the angular momentum of the incoming beam upstream of the RTFB section.

V. REMOVAL OF ANGULAR MOMENTUM AND FLAT-BEAM GENERATION

To remove angular momentum, it is necessary to apply a torque on the beam. A quadrupole can exert a net torque only on an incoming asymmetric beam. Thus more than one quadrupole is needed to remove the angular momentum of an cylindrically symmetric incoming beam. A first quadrupole followed by a drift space will introduce asymmetry in the x - y space, while the other quadrupoles downstream are properly tuned to apply a total net torque such that the angular momentum is removed at the exit of the quadrupole section. For the series of measurements and simulations presented in this section, a set of three skew quadrupoles (S2, S3, S5 in Fig. 1) are used to remove the angular momentum and generate a flat beam.

Given the photoinjector parameters, numerical simulations of the beamline (from the photocathode up to the entrance of the RTFB transformer) are performed using ASTRA. The four-dimensional phase-space coordinates are propagated downstream of the transformer using a linear transfer matrix. The initial values of the skew quadrupole strengths are those derived, under the thin-lens approximation, in Reference [28]. They are then optimized, using a least-square technique, to minimize the x - y coupling terms of the beam matrix at the exit of the transformer. The final optimized quadrupole strengths are used for subsequent ASTRA simulation of the beam dynamics through the RTFB transformer.

Further empirical optimization around the predicted values is generally needed to insure the angular momentum is totally removed, as inferred by observation of the x - y coupling at several locations downstream of the RTFB section. Evolution of transverse density throughout the RTFB section is in good agreement with expectations from simulations, as shown in Fig. 7. Each of the top six photos is a superposition of 5 bunches with charge of 0.55 ± 0.10 nC. In the sequence of measurements and simulations presented there, the incoming round beam (X3) is transformed into a flat beam characterized by the large asymmetry (X7 and

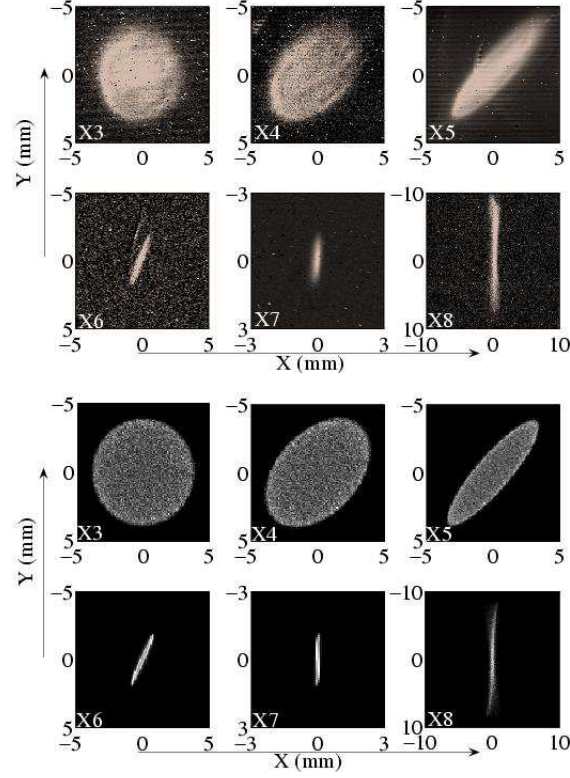


FIG. 7: Measured (top six photos) and simulated (bottom six plots) beam transverse density evolution in the RTFB section. The consecutive plots correspond to locations X3, X4, X5, X6, X7 and X8 shown in Fig. 1.

X8). The mechanical angular momentum is removed: there is no noticeable shearing as the beam propagates from X7 to X8.

VI. CONCLUSION

We have experimentally explored some parametric dependencies of angular momentum for an angular-momentum-dominated electron beam produced in a photoinjector. The results obtained are in good agreement with theoretical expectations, giving us some confidence in our understanding of the angular-momentum-dominated beam.

VII. ACKNOWLEDGEMENTS

We wish to express our gratitude to H. Edwards for her many valuable suggestions and stimulating discussions during the experiment, and for her constant support. We are grateful to D. Edwards for his comments on the manuscript and his leadership in the first flat beam demonstration experiment. We are indebted to C. Bohn of Northern Illinois University for carefully reading and commenting on the manuscript. We thank M. Hüning, K. Desler for their help in the operation, and W. Muranyi, M. Heinz, M. Rauchmiller, R. Padilla, P. Prieto and B. Degraff for their excellent technical support. This work was supported by Universities Research Association Inc. under contract DE-AC02-76CH00300 with the U.S. Department of Energy, and by NICADD.

-
- [1] I. Ben-Zvi *et al.*, in *Proceedings of the 2003 Particle Accelerator Conference, Portland, Oregon* (IEEE, Piscataway, NJ, 2003), pp. 39-41.
 - [2] Ya. Derbenev *et al.*, *Fizika Plasmy* **4**, 492-500 (1978).
 - [3] G. I. Budker *et al.*, *IEEE trans. Nucl. Sci.* **NS-22**, 2093-2097 (1975).
 - [4] R. Brinkmann, Y. Derbenev and K. Flöttmann, *Phys. Rev. ST Accel. Beams* **4**, 053501 (2001).
 - [5] Ya. Derbenev, University of Michigan Report No. UM-HE-98-04, 1998.
 - [6] K. Yokoya and P. Chen, in *Proceedings of the 1989 Particle Accelerator Conference, Chicago, IL* (IEEE, New York, NY, 1989), pp. 1438-1440.
 - [7] J. Corlett *et. al*, in *Proceedings of the 2002 European Particle Accelerator Conference, Paris, France* (EPS-IGA and CERN, Geneva, 2002), pp. 668-670.
 - [8] K.-J. Kim, private communications; C. Bohn *et. al*, unpublished, available at <http://nicadd.niu.edu/presentations/BohnFNPLspeoi.doc>.
 - [9] Y. Zhang, Ya. Derbenev, J. Boyce and R. Li, in *Proceedings of the 2003 Particle Accelerator Conference, Portland, Oregon* (IEEE, Piscataway, NJ, 2003), pp. 941-943.
 - [10] D. Edwards *et al.*, in *Proceedings of the XX International Linac Conference, Monterey, CA*, pp. 122-124 (2000).
 - [11] D. Edwards *et al.*, in *Proceedings of the 2001 Particle Accelerator Conference, Chicago, IL* (IEEE, Piscataway, NJ, 2001), pp. 73-75.

- [12] See for example, M. Reiser, *Theory and Design of Charged Particle Beams* (John Wiley & Sons, inc., 1994), pp. 33-35.
- [13] A. Burov and V. Danilov, FNAL Report No. TM-2043, 1998.
- [14] R. Brinkmann, Y. Derbenev and K. Flöttmann, DESY Report No. TESLA 99-09, 1999.
- [15] A. Burov, S. Nagaitsev and Ya. Derbenev, Phys. Rev. E **66**, 016503 (2002).
- [16] K.-J. Kim, Phys. Rev. ST Accel. Beams **6**, 104002 (2003).
- [17] M. Reiser, *Theory and Design of Charged Particle Beams* (John Wiley & Sons, inc., 1994). We start from Eq. (5.218), the second term vanishes for a drift space. Adding the canonical angular momentum term, which resembles the emittance term (see Eq. (4.80)), we obtain Eq. (5) of the present paper. See also S. Lidia, Lawrence Berkeley National Laboratory Report No. 56558, 2004 (to be published).
- [18] Y.-E Sun and P. Piot, Fermilab Beams Document, Beams-doc-1254-v1, 2004 (unpublished). Available at <http://beamdocs.fnal.gov>.
- [19] S. Lidia, in *Proceedings of the 2003 Particle Accelerator Conference, Portland, Oregon* (IEEE, Piscataway, NJ, 2003), pp. 2089-2091.
- [20] B. Aune *et al.*, Phys. Rev. ST Accel. Beams **3**, 092001 (2000).
- [21] C. Lejeune and J. Aubert, Adv. Electron. Electron Phys., Suppl. **13A**, 159 (1980).
- [22] P. Piot, G. A. Krafft, R. Li and J. Song, *Proceedings of the XIX International Linac Conference, Chicago, IL*, pp. 684-688 (1998).
- [23] H. Wiedemann, *Particle Accelerator Physics: Basic Principles and Linear Beam Dynamics* (Springer-Verlag, 1999), pp. 157-158.
- [24] J. H. Billen and L. M. Young, in *Proceedings of the 1993 Particle Accelerator Conference, Washington DC* (IEEE, Piscataway, NJ, 1993), pp. 790-792.
- [25] J.-P. Carneiro, Ph.D. thesis, Université de Paris - Sud, 2001.
- [26] Y.-E Sun *et al.*, in *Proceedings of the 2003 Particle Accelerator Conference, Portland, Oregon* (IEEE, Piscataway, NJ, 2003), pp. 2682-2684.
- [27] K. Flöttmann, “ASTRA: A Space Charge Tracking Algorithm”, user manual available at http://www.desy.de/~mpyflo/Astra_dokumentation.
- [28] E. Thrane *et al.*, in *Proceedings of the XXI International Linac Conference, Gyeongju, Korea* (Pohang Accelerator Laboratory, Pohang, Korea, 2002), pp. 308-310.
- [29] NICADD is an acronym for Northern Illinois Center for Accelerator and Detector Develop-

ment.